Damage and Failure of Blast Loaded Fiber-Reinforced Composite Laminates Considering Material and Geometric Nonlinearities

Romesh C. Batra

1   Introduction

As summarized in the World-Wide Failure Exercise papers [1, 2] there are very few failure theories that accurately simulate damage initiation and propagation in unidirectional fiber-reinforced composites deformed under quasi-static loads. Transient problems involving shock loads are even more challenging because the propagation of deformation through a heterogeneous medium necessarily involves interactions among incident waves and those reflected from interfaces between distinct materials. There is a huge difference among acoustic impedances of fibers, the matrix, and the medium surrounding the structure. Furthermore, fibers are usually transversely isotropic with much higher modulus along the fiber axis than that in the transverse direction implying that wave speeds in fibers along and across their axes are quite different. Even though one can simulate these effects by studying 3-dimensional (3-D) deformations at the constituent level, the computational effort for a real size structure is prohibitively large because of the tiny time-step size needed to find a stable numerical solution. The consideration of damage initiation and propagation further stretches the extent of computational resources required for analyzing the problem. Studying experimentally transient deformations of blast loaded sandwich structures is equally challenging since taking in-situ strain and temperature measurements require using noncontacting, mostly optical, instruments. Focusing these instruments at critical locations requires a priori knowledge of points/regions of failure initiation. Thus, experimentalists, theoreticians, and numerical analysts need to collaborate closely for a comprehensive analysis of the problem.

R. C. Batra (✉)
Department of Biomedical Engineering and Mechanics,
Virginia Polytechnic Institute and State University, M/C 0219, Blacksburg,
VA 24061, USA
e-mail: rbatra@vt.edu

An often-used strategy to simplify the problem is to homogenize material properties of the composite by using a micro-mechanics approach, and study transient deformations of the homogenized structure. This mitigates problems of wave reflections from fiber/matrix interfaces and of wide differences in wave speeds in the two materials. However, it replaces inhomogeneous face sheets and either a foam or a honeycomb core by homogenized media and removes stress singularities at contact surfaces between the different materials. Thus, one cannot accurately capture points of failure initiation especially with a stress- or a strain-based failure criterion. For using failure criteria at the constituent level, one can use a dehomogenization technique to find stresses and strains at the constituent level from those at the macro-level. Results depend upon the micro-mechanics approach, the failure initiation criteria, the ultimate failure or the structure collapse criteria, and the technique adopted for tracking failure propagation.

In numerical work, one usually simulates failure propagation by adopting one of the following techniques: deleting failed elements, releasing nodes where the material has failed, using singular surfaces, and employing a cohesive zone model (CZM). It is quite challenging to compute mesh-independent results unless the problem formulation involves a material characteristic length whose value cannot be easily ascertained.

Blast and water slamming loads on a structure induce large deformations necessitating the consideration of all material and geometric nonlinearities. Governing equations in the Lagrangian (or the material) description of motion involve nonlinear strain-displacement relations and those in the Eulerian (or the spatial) formulation have the particle acceleration as a nonlinear function of the particle velocity. Furthermore, the stress–strain relation is generally nonlinear in either formulation, and one must use materially objective (or frame-indifferent) constitutive relations. The time-step size for computing a stable solution of the governing equations must satisfy the Courant–Friedrichs–Levy (CFL) condition.

A possibility is to analyze deformations of the structure by modeling it as a plate/ shell. Reissner [3] and Koiter [4] have emphasized the need to consider both transverse shear and transverse normal deformations. Reissner stated in 1947 that for a sandwich plate with $(t_f E_f)/(h_c E_c) \gg 1$ both transverse shear and transverse normal deformations should be considered. Here, t_f and E_f (h_c and E_c) equal, respectively, the thickness and the longitudinal modulus of the face sheet (core). Based on the energy considerations Koiter [4] recommended that any refinement of the Love first approximation theory must simultaneously consider both transverse shear and transverse normal stresses. Vel and Batra [5] have provided the exact solution for thermally loaded linearly elastic plates with material moduli only varying in the thickness direction. For plates with length/thickness = 5, they found that the transverse deflection computed with the classical plate theory, the first-order shear deformable theory and the third-order shear deformable theory deviates, respectively, from the exact solution by 26%, 26% and 28%. These large errors could be due to neglecting the transverse normal strain in the three theories. For the problem studied by Vel and Batra [5], Qian et al. [6] found that a fifth-order shear and normal deformable plate theory gives results very close to the analytical

solution of the problem. For 100 K temperature difference between the top and the bottom surfaces of the plate, the deflection of the centroid of the top surface equaled twice of that of the centroid of the bottom surface signifying an average transverse normal strain of $\sim 10^{-3}$. These examples signify the need for considering transverse normal deformations for moderately thick plates/shells.

We have considered material and geometric nonlinearities and simulated damage initiation and propagation and the consequent material degradation at the constituent level while analyzing transient 3-D deformations of composite laminates. The delamination between adjacent plies is modeled with a nodal-release technique. However, for sandwich shells subjected to water slamming loads we have used a layerwise third-order shear and normal deformable plate theory (TSNDT) and simulated mixed-mode delamination with a CZM. In each case, the failed material is not allowed to heal. The interpenetration of the material across an adjoining surface is prevented by joining "contacting" nodes with a spring that is very stiff in compression but weak in tension. We describe below some of the results from our two previously published papers.

2 Failure of Fiber-Reinforced Composite Laminate Due to Blast Loads

2.1 Material Models

2.1.1 Constitutive Relation

It is common to model, e.g., see [7, 8], the material nonlinearity by using a linear relation between the second Piola-Kirchhoff stress tensor, $\mathbf{S}$, and the Green-St. Venant strain tensor, $\mathbf{E}$. That is,

$$S_{ij} = C_{ijkl}E_{kl}, \quad i,j,k,l = 1,2,3 \tag{1}$$

where $\mathbf{C}$ is the matrix of elasticities. The material described by Eq. (1) is called St. Venant-Kirchhoff. Here and below, a repeated index implies summation over the range of the index. We note that $\mathbf{S}$ has no physical meaning but is convenient to use, $\mathbf{E}$ includes all nonlinear terms in displacement gradients, and $\mathbf{S}$ and $\mathbf{E}$ are work-conjugate tensors. The stress–strain relation (1) is materially objective, and one can easily implement it in a software. From $\mathbf{S}$ and displacement gradients, one finds the true or the Cauchy stresses needed to ascertain damage initiation at a point.

A unidirectional fiber-reinforced lamina, modeled as a transversely isotropic material with the fiber along the axis of transverse isotropy, has five material constants. With $\mathbf{S}$ and $\mathbf{E}$ written as 6-D vectors, values of elasticities in the 6×6 matrix of material parameters are such that the matrix is positive-definite. For simple extensional deformations of a cylindrical isotropic body made of the St. Venant-Kirchhoff material, the structure becomes unstable in compression when

the final length/initial length (or the axial stretch) equals 0.577 irrespective of values of material elasticities [9]. For simple shear deformations, this material exhibits strain hardening because the slope of the shear stress versus the shear strain curve increases with an increase in the shear strain [9]. For a transversely isotropic material loaded along the axis of transverse isotropy, the prismatic cylinder will become unstable at a compressive axial strain whose value depends upon the material elasticities.

2.1.2 Damage Modes and Initiation Criteria

Hassan and Batra [10] presumed that elasticities of the St. Venant-Kirchhoff material degrade with an increase in the damage, and deduced the degradation relations by using the mechanics of materials approach. They considered three internal variables—one each for fiber breakage, matrix cracking, and fiber/matrix debonding. The failure in a mode ensues when the corresponding internal variable reaches a material-dependent critical value. They found expressions for the work conjugate of an internal variable, called the thermodynamic force, by using the Clausius–Duhem inequality, and for the energy dissipated in each failure mode. They determined values of material parameters from the test data of Kyriakides et al. [11].

Hassan and Batra [10] postulated a delamination surface described by a homogeneous quadratic function of the tensile transverse normal and the transverse shear stresses acting at a point on an interface between two adjacent plies. Each stress component is normalized by its value at delamination initiation. Mixed-mode delamination can occur at the interface when the transverse normal stress is tensile but only sliding prevails when it is compressive. The energy dissipated during delamination is calculated from the energy balance, i.e., subtracting from the work done by external forces the total strain energy of elastic deformations and energies dissipated due to fiber breakage, matrix cracking, and fiber/matrix debonding.

2.2 Mathematical Model

The problem is formulated in the Lagrangian description of motion using a fixed set of rectangular Cartesian coordinate axes. With $\mathbf{x}$ and $\mathbf{X}$ denoting, respectively, the position vectors of a material point in the current and the reference configurations, and t the present time, equations governing deformations of a material point are

$$\rho_R \ddot{u}_i = \left[(\delta_{i\alpha} + u_{i,\alpha})(C_{\alpha\beta\gamma\delta}E_{\gamma\delta}) \right]_{,\beta}, \ \ i, \ \alpha = 1, 2, 3 \tag{2}$$

In Eq. (2), $\mathbf{u} = \mathbf{x} - \mathbf{X}$, is the displacement of the material point $\mathbf{X}$, ρ_R the mass density in the reference configuration, and $\delta_{i\alpha}$ the Kronecker delta. A superimposed

dot indicates material time derivative, and a comma followed by α implies partial differentiation with respect to X_α.

Boundary conditions pertinent to a test set-up, initial conditions (usually zero displacements and null velocities), Eq. (2), and the nonlinear strain-displacement relations provide three nonlinear partial differential equations (PDEs) for finding **u** as a function of **X** and t.

2.3 Computational Model

We use the Galerkin method to derive a weak form of Eq. (2) that reduces nonlinear PDEs to nonlinear ordinary differential equations (ODEs) in time. We employ 8-node brick elements, evaluate integrals on an element with the $2 \times 2 \times 2$ Gauss quadrature rule, integrate the resulting ODEs with respect to time t by using the freely available subroutine LSODE (Livermore Solver for ODEs) and set in LSODE the relative and the absolute error tolerance $= 1 \times 10^{-9}$.

2.3.1 Simulation of Material Failure

From the computed nodal displacements, we ascertain values of damage parameters at each integration point within an element. When a damage initiation criterion for fiber breakage, matrix cracking, and/or fiber/matrix debonding is satisfied at an integration point, we gradually degrade values of the relevant elastic constants there till they essentially become zero (i.e., very small as compared to that of the intact material) at damage parameter $= 1$. We do not delete the element from the analysis even when the material at all its eight integration points has failed. Thus, it has kinetic energy but negligible strength and essentially zero stresses. We refer the reader to Ref. [10] for the degradation of elasticities, and evolution equations for the damage parameters.

We simulate delamination by using the nodal-release criterion, and prevent non-interpretation of materials across an interface by connecting their corresponding two nodes with a spring element that is weak in tension but stiff in compression. The postulated constitutive relation for the spring is:

$$F = k\,z_n$$
where,
$$k = \begin{pmatrix} 0, & z_n/z_0 \geq 0, \\ E_3 l \left[1 + (\eta E_3 - 1)\left(\frac{z_n}{z_0}\right)^2\right], & -1 \leq z_n/z_0 < 0, \\ \eta E_3 l, & z_n/z_0 < -1. \end{pmatrix} \tag{3}$$

Here, $F(z_n)$ is the normal force (relative displacement) between the two nodes, E_3 Young's modulus of the composite in the X_3-direction, l a characteristic length, and η a constant. Note that the value of l does not affect the mesh-dependence of results.

2.3.2 Verification of the Code

We verified the code by using the method of fictitious body forces or equivalently the method of manufactured solutions [13]. We also compared computed results for a few simple problems, such as wave propagation in a bar, with their analytical solutions. It ensures that the code correctly solves the governing equations but does not ensure that it incorporates all of the relevant physics of the problem.

2.3.3 Validation of the Mathematical Model

We compared with the test data computed results for configurations and loading conditions different from those used to deduce values of material parameters. The two sets of results agreed well with each other implying that the mathematical model incorporates in it most of the relevant physics of the problem.

2.4 Results

We present here a few results for the problem schematically shown in Fig. 1 and borrowed from Ref. [12] wherein values of material and other parameters are listed. The 22 cm $\times$ 22 cm $\times$ 1 cm unidirectional fiber-reinforced 4-ply panel with each ply 0.25 cm thick, clamped on all edges, is divided into 8-node brick elements with finer elements in the central portion. In practical applications, a thick laminate will

Fig. 1 Schematic sketch of the problem analyzed; reproduced from [12]
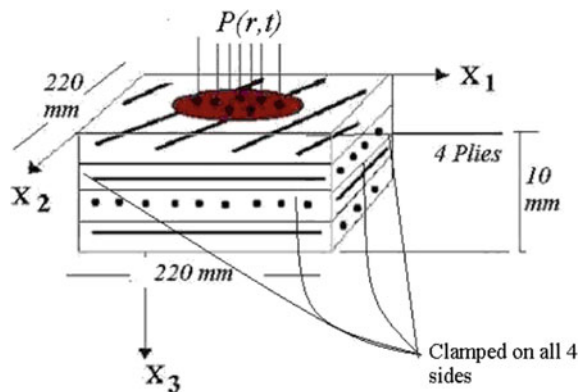
have 10^3 or more layers. The four-layer laminate studied in [12] was used to illustrate the theory within the available computational resources and the project duration.

We simulate the blast load due to underwater explosion by applying a time-dependent pressure field on the top surface of the specimen. The pressure variation with time t and the distance, r, from the centroid of the top surface of the panel has the expression

$$P(r,t) = P_{\max}e^{-t/\lambda}(-0.0005r^4 + 0.01r^3 - 0.0586r^2 - 0.001r + 1), \quad t > 0. \quad (4)$$

In Eq. (4), $P_{\max}$ is the peak pressure in the shock front, t the time elapsed since the arrival of the shock wave, and λ the decay time constant. Cole [14] has given expressions for the peak pressure, P_{max}, and the decay constant, λ, in terms of the weight, material of the explosive, and the standoff distance. The spatial variation of $P(r,t)$ is a fit to the test data of Türkmen and Mecitolu [15]. The applied pressure is representative of an explosive event and does not necessarily correspond to the values measured in a test.

2.4.1 Effect of the Finite Element Mesh

For one loading, the laminate maximum centroidal deflection computed with the four FE meshes, $20 \times 20 \times 4$ (2,205 nodes), $20 \times 20 \times 8$ (3,969 nodes), $40 \times 40 \times 4$ (8,405 nodes), and $40 \times 40 \times 8$ (15,129 nodes), till $t = 230$ μs, differed at most by 4.8%. The maximum tensile (compressive) principal stress in the laminate equaled 1.393, 1.323, 1.234, and 1.246 GPa (−0.885, −0.894, −0.917, and −1.027 GPa) for the four FE meshes, and the total work done to deform the body equaled 378, 408, 398, and 405 J. By examining time histories (not exhibited here) of the deflection at centroids of planes $X_3 = 0$ (bottom surface), $X_3 = 0.5$ cm (midsurface), and $X_3 = 1$ cm (top surface) we found that the deflections at these three points are very close to each other. It is due to the high speed of elastic waves in the transverse direction and very small laminate thickness.

The results given below are with the $20 \times 20 \times 4$ elements mesh.

2.4.2 Effect of Fiber Orientation

For each ply making the same fiber angle θ with respect to the global X_1-axis aligned along a panel edge, we have computed results for $\theta = 0°$, 10°, 30°, 45°, 60°, 75°, and 90°. Although the body is initially homogeneous, it becomes inhomogeneous because of the different damage evolved at various points, and the dependence of material properties upon the damage. As reported in [12], the fiber orientation angle has the most (least) effect on the time of initiation of the fiber/matrix debonding (the fiber breakage). However, the time of initiation and the

complete failure due to fiber breakage at specimen's centroid is virtually independent of the fiber orientation angle.

2.4.3 Fiber/Matrix Debonding

Fringe plots of the fiber/matrix debonding damage variable at t = 54, 108, 148, and 188 µs, displayed in Fig. 2, reveal that the debonding starts from edges perpendicular to the fibers and propagates along the fibers and toward the center. Plots of the time histories of the evolution of the debonding damage variable at centroids of the top, the middle, and the bottom surfaces of the laminate given in [12] suggest that the debonding instantaneously propagates in the thickness direction.

2.4.4 Matrix Cracking

By studying fringe plots of the matrix cracking damage variable at four times Hassan and Batra [12] concluded that the matrix cracking begins at approximately 108 µs at the bottom surface centroid and propagates faster along the fibers than in the transverse direction. These results agree with the experimental observations of Luo et al. [16].

We have exhibited in Fig. 3 fringe plots of the matrix cracking damage variable. These suggest that the matrix cracking ensues from points on clamped edges of the top surface that are parallel to the X_1-axis, and propagates inwards. The cracked matrix region on the top surface is centered about the X_2-axis and that on the bottom surface around its centroid as experimentally observed by Mouritz's [17]
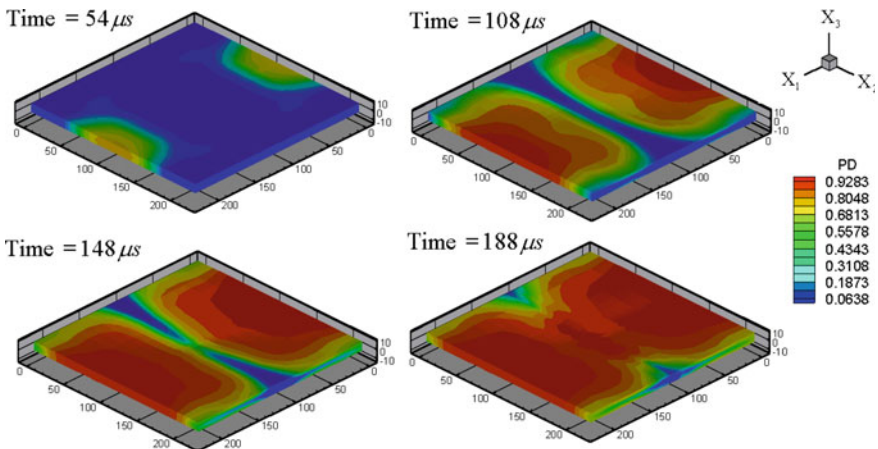

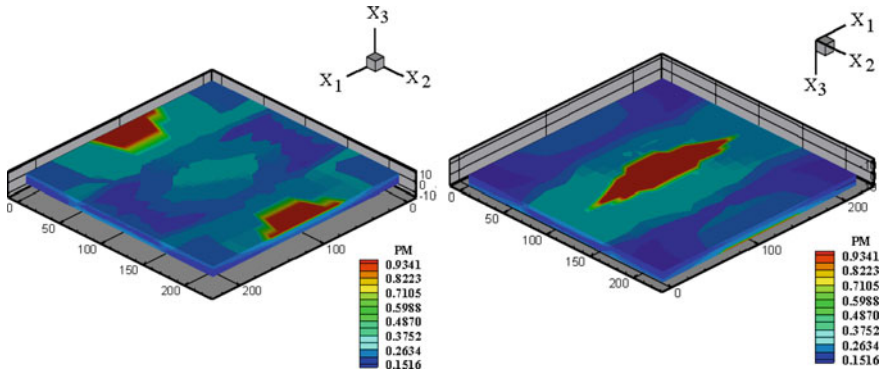**Fig. 2** Fringe plots of the fiber/matrix debonding damage variable, PD, at four different times; reproduced from [12]

Fig. 3 Fringe plots of the matrix cracking damage variable, PM, at t = 160 μs; left: top surface; right: bottom surface; reproduced from [12]

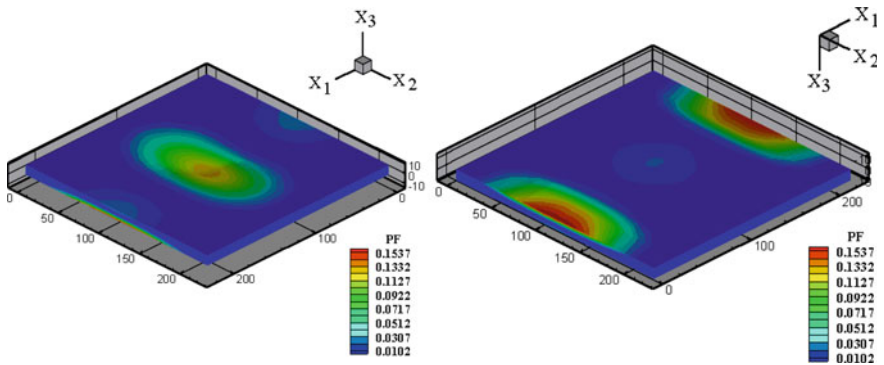**Fig. 4** Fringe plots of the fiber breakage damage variable, PF, at time = 160 μs; left: top surface; right: bottom surface; reproduced from [12]

who attributed it to high tensile bending stresses developed on the back surface. A compressive wave reflected from the traction-free back surface as a tensile wave induces more damage there causing the matrix cracking to initiate first on the bottom surface. The spalling failure mode, not considered here, can ensue at points on the bottom surface.

2.4.5 Fiber Breakage

We have depicted fringe plots of the fiber breakage damage variable at t = 160 μs in Fig. 4. These suggest that the fiber breakage is concentrated at points along the X_2-axis that are near the specimen's center. Similar to the damage variable for the matrix cracking, the damage variable for the fiber breakage also increases suddenly

from essentially 0.0 to 1.0. The time histories of the fiber breakage damage variable are given in [12].

2.4.6 Delamination Between Adjoining Layers

We have plotted in Fig. 5 fringe plots of the fiber/matrix debonding damage variable on planes $X_1 = 110$ mm, and $X_2 = 110$ mm for the 0^0 plies and $t = 220$ μs. The delamination between adjoining layers, indicated by solid lines, initiates from more than one point, not necessarily simultaneously, on an interface between two adjoining layers since these solid lines are not continuous through the entire laminate. The delamination started earliest at 128 μs for fiber orientations of 0° and 90°, and latest at 140 μs for the 45° fiber orientation.

2.4.7 Energy Dissipation Versus the Fiber Orientation Angle

Figure 6 displays the energy dissipated in the four failure modes and the total work done by external forces for different fiber orientation angles. In every case, the kinetic energy generally equals 20% of the total work done by external forces and the energy dissipated due to matrix cracking is negligible relative to that in other three damage modes. This is because the elastic moduli of the matrix are very small as compared to those of the fiber. The energy dissipated due to delamination increases but that due to fiber/matrix debonding and matrix cracking decreases as the fiber orientation angle is increased from 0° to 45°.

From results exhibited in Fig. 6, we find composite's *Figure of Merit* defined as the percentage of the work done by external forces that is dissipated in different failure modes. This metric suggests that clamped unidirectional AS4/PEEK
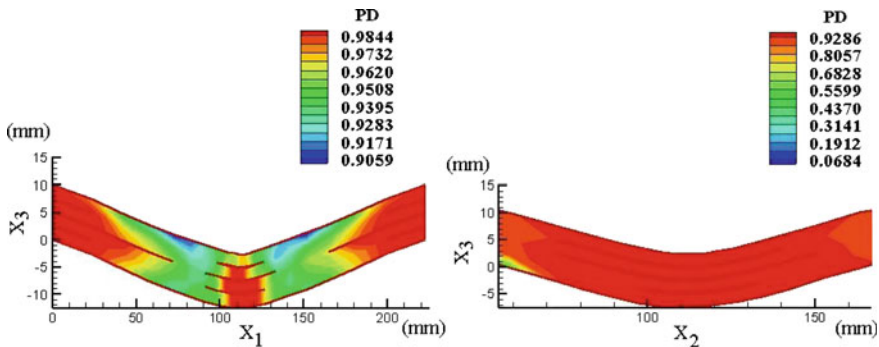

Fig. 5 At t = 220 μs, delamination/sliding between adjoining plies indicated by solid lines, and fringe plots of the fiber/matrix debonding damage variable, PD, on cross-sections $X_2 = 110$ mm (left), and $X_1 = 110$ mm (right); reproduced from [12]
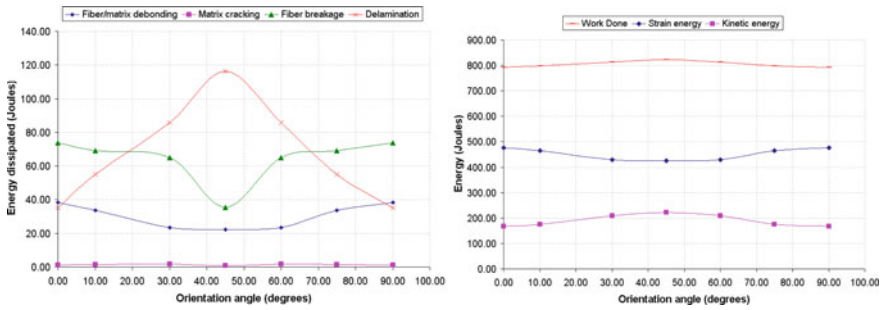
Fig. 6 Variation with the fiber orientation angle of (left) the energy dissipated in different failure modes and (right) total work done, strain energy, and kinetic energy; reproduced from [12]

composites with fiber orientations between 30° and 60° are equally effective in resisting explosive loads.

2.5 Limitations of the Model

The proposed model does not account for fiber pull out, fiber kinking, fiber buckling, and matrix crushing. The loading used to analyze the problem is a good approximation when the explosive charge is located far from the laminate. The mathematical model is not valid for composites reinforced with randomly distributed either short fibers or particulates, metal-matrix composites, and sandwich structures.

3 Delamination in Sandwich Hulls Due to Local Water Slamming Loads

We study local water slamming characterized by a large hydrodynamic load of short duration but sufficiently high intensity to cause significant structural damage, e.g., see Faltinsen [18]. In practical problems, the hull is generally curved and deformable. Hull's deformations affect the fluid motion and the hydroelastic pressure acting on the fluid/hull interface. Charca and Shafiq [19], amongst others, have experimentally studied the failure of sandwich composite panels including core shear, delamination, and damage of the face sheets due to water slamming.

We have exhibited in Fig. 7 a schematic sketch of the problem studied. The sandwich hull composed of stiff face sheets and a flexible core experiences localized slamming pressure. For hull speeds of 10 m/s, viscous effects in water are often neglected and the water compressibility plays a noticeable role only for a very short duration after the hull contacts the water. We assume the water to be
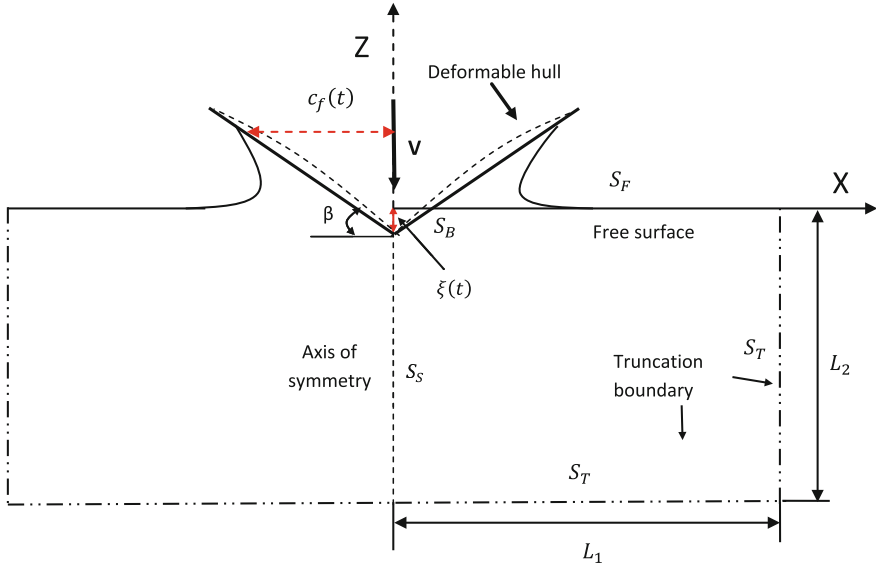
Fig. 7 Schematic sketch of the water slamming problem studied; reproduced from [20]

incompressible, inviscid, and undergoing irrotational motions. While analyzing deformations of a sandwich structure, as recommended by Reissner [3] and Koiter [4], we consider transverse normal and transverse shear deformations and use the CZM as well as coupled boundary element (BE) and FE methods to delineate delamination between adjacent plies induced by the hydroelastic pressure. We employ the BEM to analyze the fluid motion and the FEM in conjunction with the TSNDT to study transient deformations of the curved sandwich hull made of a St. Venant-Kirchhoff material. The continuity of the pressure and of the normal component of velocity at the water/hull interface couples hull's deformations with the water motion. The Rayleigh damping for the structure incorporated into the problem formulation reduces oscillations in the hydrodynamic pressure on the solid/fluid interface.

The assumptions of irrotational motion and incompressibility of the fluid imply that there exists a velocity potential φ such that the fluid velocity $v = -\nabla\varphi$, where ∇ is the spatial gradient operator in the XZ-plane, and that φ satisfy the Laplace equation. The Laplace equation under pertinent boundary conditions is solved by the BEM with the fluid/structure interface updated after every time increment. The Bernoulli equation relating the pressure at a point to the kinetic energy density there is used to find the pressure.

We use the TSNDT and the FEM to analyze transient deformations of the St. Venant-Kirchhoff hull, and use the CZM for simulating delamination between adjacent layers of distinct materials.

The Table 1 and results described below are borrowed from Ref. [20]. In Table 1, we have compared features of our coupled BE-FE software with those of

Table 1 Comparison of LSDYNA and coupled BE-FE approaches for the water slamming problem

	LSDYNA	BE-FE methods
Fluid penetration into solid	Yes	No
Hull pressure oscillations	Yes	No
Dependence of results on contact algorithm	Yes	No
Water jet delineation	Difficult	Easy
Fluid flow assumptions	Compressible	Incompressible and irrotational
Finding strain rates in the fluid domain	Easy	Difficult

Table 2 Values of material parameters of the sandwich hull

	C_{1111} (GPa)	C_{1133} (GPa)	C_{3333} (GPa)	C_{1313} (GPa)	Mass density (kg/m^3)
Face sheet	140.3	3.77	9.62	7.10	31,400
Core	3.77	1.62	3.77	1.08	150

the commercial code, LSDYNA. It is clear that the in-house developed code avoids fluid penetration into the hull.

3.1 Water Slamming of Linearly Elastic Straight Sandwich Hull

We now analyze plane strain deformations of a clamped–clamped linearly elastic straight sandwich hull of deadrise angle, $\beta = 5°$, hull length = 1 m, thickness of each face sheet = 1.2 cm, core thickness = 3.0 cm, downward impact velocity = 10 m/s, and values of material parameters listed in Table 2. The face sheet mass density includes the dead weight of the ship. We discretize the sandwich beam into 60 uniform 2-node elements and the boundary of the 5 m × 15 m fluid domain into 2-node elements. We successively refined the mesh on the fluid boundary to get a converged solution.

For the Rayleigh damping coefficient $\alpha = 5 \times 10^{-6}$ and 5×10^{-7}, the time histories of the pressure at $y_1 = 0.35$ m plotted in Fig. 8 reveal a significant reduction in oscillations in the pressure and miniscule difference in results for the two values of α. The pressure computed without (with) using the added mass method exhibits (no) oscillations at $t = 4$ ms. The three pressure variations on the hull at $t = 2.72$, 4.79, and 5.75 ms are from the present BE-FE method, Qin and Batra's [21] semi-analytical approach, and the Das and Batra's [22] numerical solution computed using LSDYNA. The modified Wagner's theory employed in
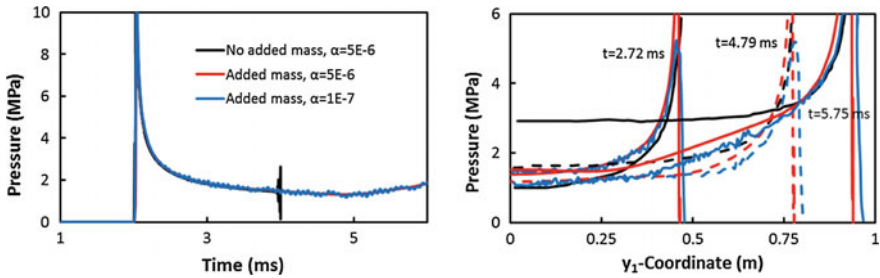
Fig. 8 For initial impact speed = 10 m/s, (left) time histories of the pressure on the hull at $y_1 = 0.35$ m for two values of the damping ratio, and with and without adding mass due to the acceleration of particles on the hull surface. The three curves overlap each other. Right: Pressure distribution on the hull at $t = 2.72$, 4.79 and 5.75 ms. Black, blue and red curves, respectively, represent results computed by Qin and Batra [20], Das and Batra [21], and the coupled FE-BE method. The y_1-axis is along the hull; reproduced from [20]

[21] gives singular pressure field and its peak value is approximated in the plot. Except for the peak pressure, the three methods give results close to each other. Hull's deformations are assumed to be infinitesimal in [21] but all geometric nonlinearities are considered in [22].

3.2 Water Slamming of Straight Sandwich Hull Made of St. Venant-Kirchhoff Material

We have simulated two water slamming problems to delineate the influence of geometric nonlinearities and hull stiffness on the hydrodynamic pressure acting on a sandwich hull. For problem 1 values of elastic constants are the same as those for the hull studied in Sect. 3.1, and for problem 2, values of all elastic parameters have been reduced by a factor of 10 and the mass density reduced to 2,000 kg/m³. For problem 2 we set each face sheet thickness = 6 mm, core thickness = 7.5 mm, and hull length = 1 m. The first fundamental frequencies for the hulls of problems 1 and 2 without considering added mass are 110 and 101 Hz, respectively. The deadrise angle and the downward velocity of the hull for both problems, respectively, equal 10° and 10 m/s. Effects of geometric nonlinearities are considered only for problem 2. The time step = 0.75 μs was used to compute results for both problems.

Time histories of the mid-span deflection depicted in Fig. 9 (left), and the pressure distribution on the hull at two different times in Fig. 9 (right) vividly illustrate that the consideration of geometric nonlinearities significantly influences hull's deformations and its interaction with the surrounding fluid. Geometric non-linearities reduce hull's mid-span deflection by 33% as compared to that found from the linear theory.
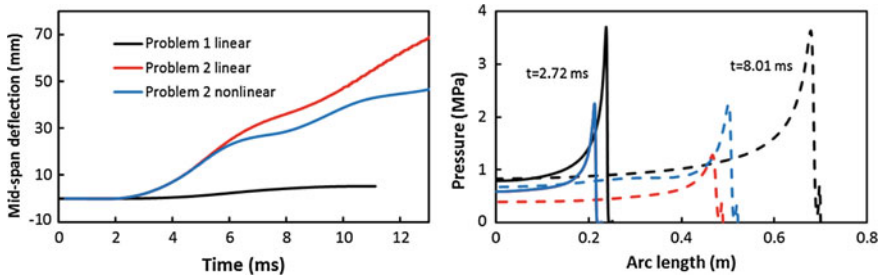
Fig. 9 Left: time histories of the mid-span deflection for the three problems studied; right: hydroelastic pressure on the hull at two different times. Black, red, and blue curves represent, respectively, results for linear problem 1, linear problem 2 and nonlinear problem 2; reproduced from [20]

Fig. 10 Pressure distribution on circular hull with $R = 5$ m (solid curves) and flat (dashed curves) hulls. Black, red and blue curves, respectively, represent results at $t = 2.72$, 4.79 and 5.75 ms; reproduced from [20]
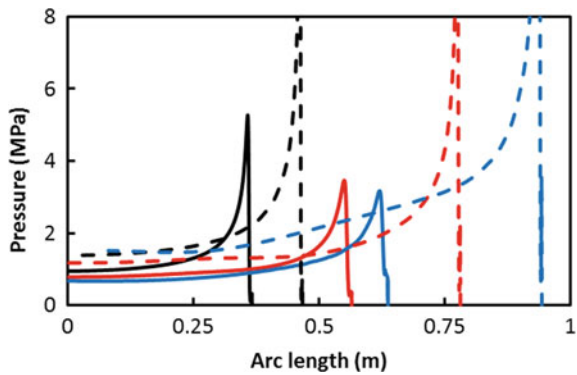
3.3 Water Slamming of Linear Elastic Circular Sandwich Hull

From the variation of the hydroelastic pressure on curved and straight hulls at three times depicted in Fig. 10, we see that the hull curvature noticeably influences the peak pressure and the pressure distribution on the hull. For each value of time, the peak pressure on the circular hull is considerably less than that on the flat hull and, as expected, occurs at different locations. The pressure distribution on the hull resembles a traveling wave with the peak pressure acting at the just wetted point, the pressure rapidly decreasing in its wake, and staying uniform over a significant part of the wetted length.

3.4 Delamination in Linearly Elastic Straight Sandwich Hull Due to Water Slamming Loads

We divide the clamped–clamped linearly elastic straight sandwich hull of length = 1 m, deadrise angle = 5° into 81 uniform 2-node elements. The geometric and material parameters, and the entry velocity for problem 1 are the same as those for the hull studied in Sect. 3.1. We set $\sigma_t^0 = \sigma_n^0 = 1$ MPa, $G_{Ic} = 625$ Jm^{-2}, $G_{IIc} = 418$ Jm^{-2}, where G_{Ic} and G_{IIc} are, respectively, the critical energy release rates for mode I and mode II failures, and σ_t^0 and σ_n^0 are the strength parameters. Values of various parameters used here are not necessarily for a real material. For problem 2, we take the thickness of each face sheet = 2 cm, core thickness = 6 cm, downward impact velocity = 10 m/s, deadrise angle = 10°, $\sigma_t^0 = 3.5$ MPa, $\sigma_n^0 = 7.1$ MPa, $G_{Ic} = 625$ Jm^{-2} and $G_{IIc} = 418$ Jm^{-2}. Values of elasticities for the core and the interface strength are listed in Table 3.

For problem 1, we have compared in Fig. 11 time histories of the deflection of the hull centroid with and without considering delamination computed using the BE-FEM with those of [21] obtained by using LSDYNA. It is clear that the two sets of results are close to each other. The hull centroid deflection considering delamination is larger than that without accounting for delamination. The reduction in sandwich hull's stiffness due to delamination increases its deflections and decreases the hydroelastic pressure on the hull surface as shown in Fig. 12.

Table 3 Values of material parameters of the sandwich hull

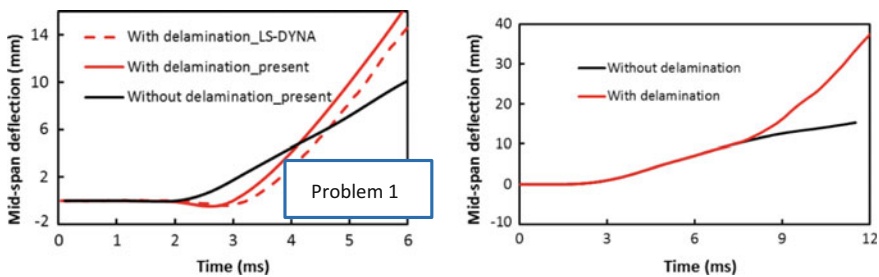|	C_{1111} (GPa)	C_{1133} (GPa)	C_{3333} (GPa)	C_{1313} (GPa)	Mass density (kg/m^3)
Face sheet	13.4	2.40	5.92	1.92	1,850
Core	0.307	1.62	0.0923	0.107	200

Fig. 11 Time histories of the straight hull centroid deflection with and without considering delamination; reproduced from [20]

In order to quantify delamination, we introduce a scalar, ω, that equals 1 (0) at a point for complete (no) delamination. For the two problems studied, we have plotted in Fig. 13 fringe plots of ω in ty_1-plane on the two interfaces. These plots
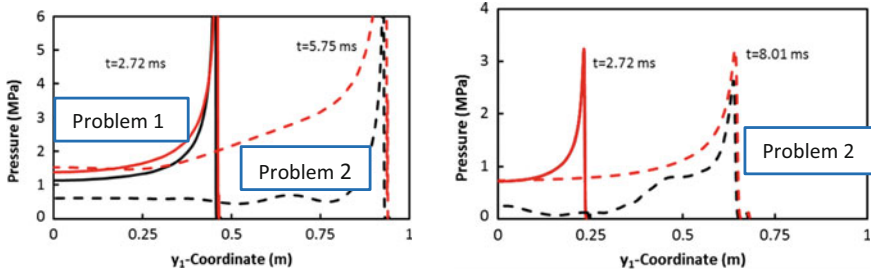

Fig. 12 Distribution of the hydroelastic pressure on the hull at two values of t. Black (red) curve represents results with (without) considering delamination. The red and black curves at $t = 2.72$ ms for problem 2 overlap as the beam has not been delaminated at this time; reproduced from [20]
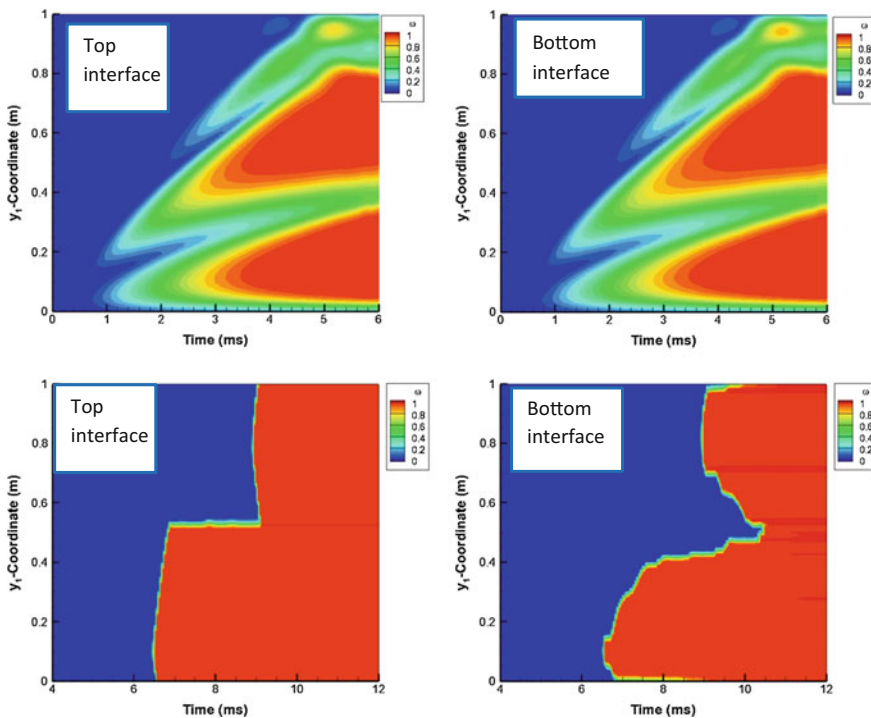

Fig. 13 Variation of the separation index ω with the y_1-coordinate and the time, on the top and the bottom interfaces for problems 1 (top 2) and 2 (bottom 2); reproduced from [20]

suggest that for problems 1 and 2 the complete delamination first occurs on both interfaces at points close to the left edge or near $y_1 = 0$ at $t = 3.6$ and 6.5 ms, respectively, and propagates to the right edge. At $t = 6$ ms, whereas most of the interfaces have been delaminated for problem 1, the delamination has not begun for problem 2. For problem 2, the two interfaces are delaminated at different rates with the top and the bottom interfaces completely delaminated at approximately $t = 9.5$ and 11 ms, respectively. The delamination process is unstable for problem 2 as evidenced by sharp increases followed by arrests in the delamination lengths.

4   Conclusions

Results presented here for the initiation and propagation of the fiber breakage, matrix cracking, fiber/matrix debonding, and delamination between adjacent plies in a clamped square composite laminate under a blast load suggest the following sequence for the failures:

  (i)   fiber/matrix debonding at edges of the bottom and the top surfaces that are perpendicular to the fibers,
 (ii)   matrix cracking at the bottom surface centroid, and at the top surface edges normal to the fibers,
(iii)   fiber breakage at the top surface edges parallel to fibers followed by that at the bottom surface centroid,
 (iv)   debonding at the bottom and the top surfaces centroids,
  (v)   fiber breakage at the top surface centroid,
 (vi)   fiber breakage at the bottom surface sides, and
(vii)   matrix cracking at the top surface centroid.

With all four plies having the same fiber orientation, the total energy dissipated in all failure modes is higher for fiber orientation angles between 30° and 60° with the panel edge than that for other fiber angles.

The slamming load on a straight sandwich hull induces delamination between stiff face sheets and the soft core with the mode II failure being unstable. The propagation of the hydroelastic pressure on the hull resembles a traveling wave with the peak pressure at the front. The pressure decay in the wake is different for intact and delaminated hulls.

References

1. Kaddour, A. S., & Hinton, M. J. (2007) The second world-wide failure exercise: Benchmarking of failure criteria under triaxial stresses for fiber-reinforced polymer composites. In *16th International Conference on Composite Materials* (pp. 2295–2312).
2. Kaddour, A. S., & Hinton, M. J. (2013). Maturity of 3D failure criteria for fiber-reinforced composites: Comparison between theories and experiments: Part B of WWFE-II. *Journal of Composite Materials, 47*(6–7), 925–966.
3. Reissner, E. (1947). Small bending and stretching of sandwich type shells. *National Advisory Committee for Aeronautics, Technical Note No.* 1832.
4. Koiter, W. T. (1960). A consistent first approximation in the general theory of thin elastic shells. In *Proceedings of IUTAM Symposium on the Theory of Thin Elastic Shells* (pp. 12–33). Amsterdam: North Holland Publishing Co.
5. Vel, S. S., & Batra, R. C. (2002). Exact solutions for thermoelastic deformations of functionally graded thick rectangular plates. *AIAA Journal, 40,* 1421–1433.
6. Qian, L. F., Batra, R. C., & Chen, L. M. (2003). Free and forced vibrations of thick rectangular plates by using higher-order shear and normal deformable plate theory and meshless local Petrov-Galerkin (MLPG) method. *Computer Modeling in Engineering and Science, 4,* 519–534.
7. Batra, R. C., & Xiao, J. (2013). Finite deformations of curved laminated St. Venant-Kirchhoff beam using layer-wise third order shear and normal deformable theory (TSNDT). *Composite Structures, 97,* 147–164.
8. Allix, O., & Corigliano, A. (1999). Geometrical and interfacial non-linearities in the analysis of delamination in composites. *International Journal of Solids and Structures, 36*(15), 2189–2216.
9. Batra, R. C. (2001). Comparison of results from four linear constitutive relations in isotropic finite elasticity. *International Journal of Nonlinear Mechanics, 36,* 421–432.
10. Hassan, N. M., & Batra, R. C. (2008). Modeling damage in polymeric composites. *Composites B, 39,* 66–82.
11. Kyriakides, S., Arseculeratne, R., Perry, E., & Liechti, K. (1995). On the compressive failure of fiber reinforced composites. *International Journal of Solids and Structures, 32*(6–7), 689–738.
12. Batra, R. C., & Hassan, N. M. (2007). Response of fiber reinforced composites to underwater explosive loads. *Composites: Part B, 38,* 448–468.
13. Batra, R. C., & Liang, X. Q. (1997). Finite dynamic deformations of smart structures. *Computational Mechanics, 20,* 427–438.
14. Cole, R. H. (1948). *Underwater explosions*. Princeton: Princeton University Press.
15. Türkmen, H. S., & Mecitolu, Z. (1999). Dynamic response of a stiffened laminated composite plate subjected to blast load. *Journal of Sound and Vibration, 221*(3), 371–389.
16. Luo, R., Green, E., & Morrison, C. (2001). An approach to evaluate the impact damage initiation and propagation in composite plates. *Composites Part B, 32,* 513–520.
17. Mouritz, A. (1996). The effect of underwater explosion shock loading on the flexural properties of GRP laminates. *International Journal of Impact Engineering, 18*(2), 129–139.
18. Faltinsen, O. M. (1993). *Sea loads on ships and offshore structures*. Cambridge, UK: Cambridge University Press.
19. Charca, S., & Shafiq, B. (2010). Damage assessment due to single slamming of foam core sandwich composites. *Journal of Sandwich Structures and Materials, 12,* 97–112.
20. Xiao, J., & Batra, R. C. (2014). Delamination in sandwich panels due to local water slamming loads. *Journal of Fluids and Structures, 48,* 122–155.
21. Qin, Z., & Batra, R. C. (2009). Local slamming impact of sandwich composite hulls. *International Journal of Solids and Structures, 46,* 2011–2035.
22. Das, K., & Batra, R. C. (2011). Local water slamming impact on sandwich composite hulls. *Journal of Fluids and Structures, 27,* 523–551.